Title

Insights into the Thermo-Hydraulic Properties of Compacted MX80 Bentonite during Hydration under Elevated Temperature

Journal

Canadian Geotechnical Journal, 0(ja)

ISSN

0008-3674

Authors

Lu, Yu

McCartney, John S

Publication Date

2023-06-24

DOI

10.1139/cgj-2022-0537

Peer reviewed

Insights into the Thermo-Hydraulic Properties of Compacted MX80 Bentonite during Hydration under Elevated Temperature

Yu Lu, Ph.D.

Postdoctoral Researcher, Dept. of Structural Engineering, Univ. of California San Diego, 9500 Gilman Dr., La Jolla, CA 92093-0085; yul204@ucsd.edu

John S. McCartney, Ph.D., P.E., F.ASCE (corresponding author)

Professor and Chair, Dept. of Structural Engineering, Univ. of California San Diego, 9500 Gilman Dr., La Jolla, CA 92093-0085; mccartney@ucsd.edu

ABSTRACT: In high-level radioactive waste geological repositories, compacted bentonite undergoes coupled thermo-hydraulic processes due to heat released from a central waste canister and groundwater imbibition from the surrounding host rock. An understanding of these processes is essential for long-term simulations radionuclide migration and canister corrosion, which requires an understanding temperature effects on the coupled thermo-hydraulic properties governing these processes. In this study, a tank-scale radial infiltration test was used to investigate water imbibition processes in compacted bentonite under a central heater temperature of 200°C that simulates high thermal gradients in a repository. Interpretation of this test focuses on evaluation of the liquid water wetting front during hydration and the interpretation of the temperature-dependent transient soil water retention curve (SWRC), thermal conductivity function (TCF), and hydraulic conductivity function (HCF). The SWRC during imbibition follows a temperature-dependent wetting path. Temperature effects on the hydraulic conductivity of bentonite in saturated conditions had the greatest effect on the shape of the HCF, with minimal temperature effects at higher suctions. The transient thermal conductivity data matched well with a new TCF linked with the SWRC shape. Although the bentonite layer was restrained, local deformations during hydration may have affected the shapes of the TCF and HCF.

KEYWORDS: MX80 bentonite; Tank test; Central heating; Radial infiltration; Unsaturated soil mechanics; Hydraulic conductivity function

INTRODUCTION

A key component of multi-barrier system used for permanent disposal of high-level radioactive waste (HLW) is the buffer/sealing material placed between the HLW canister and the surrounding host rock to create a zone of low permeability that separates the HLW from the surrounding environment (Pusch 1979; Börgesson et al. 1994; Lloret et al. 2003; Kim and Dixon 2013; Schanz and Al-Badran 2014). Compacted bentonite is often used as the buffer/sealing material owing to its ultra-low hydraulic conductivity, high cation exchange capacity, swelling capacity, along with adequate mechanical properties (Pusch 1979; Komine and Ogata 1994; Marcial et al. 2002; Villar 2005; Lu et al. 2021). Once compacted within the repository, a temperature gradient is expected to be established in the bentonite between the high temperature container associated with decay of nuclides and the stable, lower temperature of the surrounding host rock. At the same time, a hydraulic gradient is expected to be established between the high initial suction within the bentonite and the hydrostatic water pressure in the host rock. Thus, combined heating and hydration under restrained volume conditions will lead to a set of coupled thermo-hydraulic processes shown schematically in Figure 1.

The hydraulic conductivity of compacted bentonite under various thermal gradients is a key variable in assessing the performance of the buffer in an engineering barrier system as it controls the liquid water transfer-related phenomena, such as over-pack corrosion, nuclide migration, or other effects (Ye et al. 2009; Wang et al. 2013). Several studies have investigated liquid water flow in compacted bentonite in both saturated conditions (Pusch 1980; Dixon et al. 1999; 2023; Ito et al. 2022; Watanabe et al. 2023) and unsaturated conditions (Mualem 1976; Kröhn 2003; Cui et al. 2008; Dai et al. 2008; Villar et al. 2012, 2014; Ye et al. 2014; Gens et al. 2021; Zeng et al. 2022). The saturated

hydraulic conductivity has been found to be dependent on the mineral composition, geometric properties of the pore channel (compactness, porosity, tortuosity, specific surface area), fluid properties (viscosity, concentration), and temperature (Johnson et al. 1994; Dixon et al. 1999). For liquid water flow in unsaturated soils, it is well established that the relationship between the hydraulic conductivity and volumetric water content (or matric suction), referred to as the hydraulic conductivity function (HCF), is related to the shape of the soil-water retention curve (SWRC) (van Genuchten 1980). The instantaneous profile method (Watson 1966) is often used to determine the value of hydraulic conductivity of unsaturated soils from transient measurements of water content and matric suction. Ye et al. (2009) used this method to investigate the unsaturated hydraulic conductivity of compacted GMZ bentonite and observed that with suction decrease under constant volume conditions, the hydraulic conductivity decreases followed by an increase after a certain suction threshold. This phenomenon was also observed for the Kunigel bentonite/sand mixture by Cui et al. (2008), who noted that this is different from the expected conclusion that the hydraulic conductivity of unsaturated soils increases with decreasing suction. Kim et al. (2019) used an axisymmetric model to perform coupled HM simulations of MX80 bentonite-sand mixture performance for 100 years under isothermal conditions. The corresponding evolutions of saturation and SWRC were presented in a follow-up study by Kim et al. (2020). For hydraulic conductivity under elevated temperature, Gens and Zandarin (2009) conducted constant volume mock-up tests on MX80 bentonite in two phases: basal heating 1:1 soil column (203 mm) at 150ºC, and then constant pressure hydrating the soil from the top boundary. Villar and Gómez-Espina (2009) performed two hydration tests on FEBEX bentonite using cylindrical cells with an inner diameter of 70 mm and a useful height of 400 mm under room and elevated (up to 100°C)

temperatures, respectively. These tests provide meaningful time history results for understanding the coupled THM behavior of bentonite, as well as a reference for subsequent simulations (e.g., Thomas et al. 2009; Vardon 2009; Abed and Sołowski 2017) and laboratory physical-modeling investigations (e.g., this study). Ye et al. (2012) conducted a test on compacted GMZ01 bentonite under confined conditions with temperatures ranging from 20 to 60°C and noticed that the hydraulic conductivity of unsaturated bentonite increases as temperature increases, at a decreasing rate with temperature rise. Due to the coupled processes expected in buffers, the effects of temperature on the HCF associated with bentonite hydration needs further study.

Many studies have also investigated the thermal conductivity of compacted bentonite, and confirmed that thermal conductivity was strongly dependent on soil structure, minerals, dry density, porosity and water content, etc. (Börgesson et al. 1994; Tang et al. 2008; Lu et al. 2020). For instance, Abootalebi and Siemens (2018) examined the thermal conductivities of MX80 and other bentonites and revealed a strong influence of water content on thermal properties. Recently, some significant progress has been made in better describing the thermal conductivity of compacted bentonite, and several thermal conductivity models have been proposed. For instance, Dong et al. (2015) presented a comprehensive review of the mathematical bases of different thermal conductivity models. While Lu and Dong (2015) proposed a closed-form TCF related to the shape of SWRC, their TCF does not converge to the maximum thermal conductivity when the soil is saturated. This issue was recently addressed in a new TCF developed by Lu and McCartney (2023) that is applied in this study.

The radial temperature gradient in the geological repository extends from the hot canister in the center through the buffer material then into the host rock. Thermal conduction will be perpendicular to the compaction direction of the bentonite. Several

studies have noted that the compaction process induces anisotropic thermal conductivity in bentonite (Lu et al. 2020). Similar inconsistencies also occurred in the water infiltration direction, since the groundwater typically infiltrates from the surrounding host rock into the bentonite blocks and canister along the radial direction, different from the commonly used specimen's axial direction in lab tests, and an anisotropic hydraulic conductivity has been confirmed in many compacted clayey soils (Boynton and Daniel 1985; Dudoignon et al. 2004). However, previous research on bentonite typically only considered the thermal and hydraulic gradients in the axial direction, which does not fully represent the radial heat transfer process in a repository. Full-scale tests with three-dimensional behavior focus have been designed or initiated, such as the "prototype repository" experiment at Äspö Hard Rock Laboratory (Svemar and Pusch 2000). While valuable in understanding actual repository construction effects, boundary conditions, and benchmarks for numerical simulations (e.g., Thomas et al., 2014), the installation and operating costs are significant. Another issue with past in-situ and mock-up studies is that the temperatures applied were typically below 150°C, while new repository conditions being explored involve waste canister temperatures up to 200°C. For example, the recently started full-scale in-situ HotBENT experiment involves a maximum heater temperature of 200°C (GTS 2022). Zheng et al. (2015, 2017) conducted coupled THMC simulations for thousands of years with maximum temperatures of 200°C. However, the thermo-hydraulic properties of bentonite used in their study were measured at room temperature. Information on how bentonite behaves at higher temperatures is desirable for optimizing repository design, space and costs (e.g., footprint, layout), and for providing more options regarding the required storage periods (GTS 2022).

This study aims at addressing this gap in the literature by investigating the thermo-

hydraulic properties of compacted bentonite during restrained hydration after approaching equilibrium at a central heater temperature of 200°C and a steep radial thermal gradient. A tank-scale test with precise control over the applied thermal and hydraulic gradients and stress state was used to evaluate the hydration process, and this paper reports new experimental data collected from the end of a heating process previously reported by Lu and McCartney (2022). This paper provides a novel contribution by using the transient measurements from the tank-scale test to validate the function form of coupled thermo-hydraulic properties developed for compacted bentonite, including a temperature-dependent transient soil water retention curve (SWRC), hydraulic conductivity function (HCF), and thermal conductivity function (TCF).

MATERIAL

The material used in this study is MX80 bentonite from Wyoming, USA, one of the most popular types of bentonites used internationally in bentonite buffer systems (Villar 2005). The American Colloid Company distributes MX80 bentonite in granular form with an initial gravimetric water content of approximately 9%. Details of the geotechnical index properties, grain size distribution curves in both granular forms using sieve testing and hydrated forms using hydrometer testing, as well as the SWRC obtained for individual specimens compacted to an initial dry density of 1.3 Mg/m^3 can be found in Lu and McCartney (2022).

EXPERIMENTAL INVESTIGATION

Experimental setup

The experimental setup in this study consists of an insulated cylindrical aluminum container, a heating system, a loading system with LVDT, a hydration system, and several embedded sensors. A picture and schematic diagram of the experimental setup

are shown in Figure 2. The aluminum tank has an internal diameter of 554.5 mm, a thickness of 16.5 mm, and a height of 477.8 mm. The upper surface of the bentonite is confined by a reinforced concrete cap with a diameter of 540 mm, a height of 57.2 mm, and a mass of 48.78 kg. Mineral wool blanket insulation with a thickness of approximately 100 mm was wrapped around the sides of the tank, below the tank, and above the concrete cap to minimize heat losses.

The heating system consists of a Watlow Firerod 2127 cartridge heating element and an EZ-ZONE PM6 temperature controller. The cartridge heating element has a diameter of 12.5 mm and a height of 102 mm in height, with a maximum power output of 1100 W. The heater temperature was maintained constant at 200°C throughout the hydration phase presented in this paper. Lu and McCartney (2022) presented data from the heating stage of this experiment and observed a sharp drop off in temperature in the bentonite with distance from the heater.

After the end of heating in the test reported by Lu and McCartney (2022), a loading system was added to restrain the bentonite to prevent swelling during hydration. The loading system consists of an Enerpac RSM500 hydraulic ram with a hand pump, a gauge, a hose, and a check valve. The hydraulic ram kit can control the soil swelling deformation by applying vertical loading, and the hydraulic ram with a capacity of 472 kN and a stroke of 16 mm, while a check valve was used to keep the hydraulic pressure constant. The floating concrete top cap (not fixed on the tank) and a reaction plate (connected to the base of the tank using threaded rods) form an integrated loading system to apply axial loads to the soil layer to prevent volume changes during bentonite hydration. The axial load was measured by an Interface Force 1220 load cell with a range of up to 222 kN. A Schaevitz 500HR linear variable differential transformer (LVDT) having a range of 25.4 mm and a sensitivity of 28 mV/V/mm was used to

monitor the vertical deformations of the bentonite layer during hydration so that the loading system could be adjusted to keep the soil volume approximately constant.

The hydration system consists of a Mariotte bottle with a volumetric capacity of 2000 ml that can apply constant water head during water flow into the soil layer. A water table is maintained at the top level of the bentonite during hydration, so hydration proceeds due to the large suction gradient established within the bentonite layer due to the initial thermally induced drying stage reported by Lu and McCartney (2022).

The thermo-hydraulic response of the bentonite layer was monitored using four TE HTM2500LFL relative humidity sensors that have an accuracy of ±3%, five Meter Teros 12 dielectric sensors that have an accuracy of ±0.01–0.02 m^3/m^3 for volumetric water content and ±0.5 °C in temperature, three Decagon KD2 Pro thermal needle probes, and three Omega Type K thermocouples at locations described in Figure 2(b). Dimensions and sensitivities of the sensors can be found in Lu and McCartney (2022). Prior to hydration, three thermal needles from Decagon devices were installed in the bentonite layer: a TR-1 single needle probe with a thermal conductivity measurement range from 0.1 to 4.0 W/(m·K) with accuracy ±0.02 from 0.1 to 0.2 W/(m·K) and ±10% from 0.2 to 4.0 W/(m·K), a KS-1 single needle probe with a measurement range from 0.02 to 2.0 W/(m·K) with accuracy ±0.01 from 0.02 to 0.2 W/(m·K) and ±5% from 0.2 to 2.0 W/(m·K), and a SH-1 dual-needle probe with a thermal conductivity range from 0.02 to 2.0 W/(m·K) with accuracy ±0.01 in thermal conductivity measurement from 0.02 to 0.2 W/(m·K) and ±10% from 0.2 to 2.0 W/(m·K). The dual-needle probe also provides volumetric heat capacity values ranging from 0.5 to 4.0 MJ/(m^3·K) with accuracy of ±10% for thermal conductivities above 0.1 W/(m·K).

Soil layer preparation and sensor location

A cross-sectional schematic with the compacted bentonite layer and instrumentation

locations is shown in Figure 2(b). The compaction conditions for the soil layer are summarized in Table 1. The MX80 bentonite in as-received conditions was first carefully mixed with water to reach a constant gravimetric water content of 12.55% and stored in a sealed container to ensure homogeneity. Then the bentonite was compacted into eight 25.5 mm-thick lifts with the goal of reaching a target height of 204 mm. However, due to the inclusion of sensors in the bentonite layer during compaction, the final thickness of the layer was 210.5 mm. The heating element was installed after the placement of the second lift in the center of the soil layer, and the third and fourth lifts were compacted around the heating element. The relative humidity sensors were placed atop the fourth lift (at the bottom of the fifth lift), and the dielectric sensors were inserted into the top of the sixth lift so that the sensing probes were within the fifth and sixth lifts, while the thermal needle probes were inserted into the top of the fifth, sixth and seventh lift (depended on the length of the probe) so that the sensing probes were within middle soil layer. One Type K thermocouple was placed out of the tank to measure room temperature, while the other two were placed at the top of the soil layer above the heating element, and at the inside edge of the container in the middle of the bentonite layer. Two layers of 13 μm-thick plastic wrap were placed on top of the bentonite layer to help maintain a constant water content before placing the concrete cap. Then, the LVDT was placed on the top of the cap to measure the vertical displacement of the entire soil layer, which was used to control the applied axial loads to ensure the volume change was minimal. While uncertainties in sensor measurements may exist under temperatures above 100 °C, the temperature at the locations of the sensors were within the manufacturer-specified ranges due to the sharp drop-off in temperature away from the central heater reported by Lu and McCartney (2022) so the measurements are expected to be within the sensor accuracy ranges reported above.

Coupled heating and hydration test

The high-temperature heating process on the compacted bentonite was started with the temperature of the heating element set to 200°C to replicate the temperature expected in the HotBENT project at the Grimsel Test Site (Zheng et al. 2015; GTS 2022). After 100-day pre-heating which allowed the soil temperatures to stabilize (as reported by Lu and McCartney (2022)), the hydration process was started using the Mariotte bottle in which the bottom of the tube exhaust pipe was set at the same level as the very top of the compacted bentonite layer (Figure 2(b)). As this paper focused on evaluation of the wetting front during hydration and the interpretation of the temperature-dependent transient SWRC and HCF, the time of starting hydration was regarded as the beginning of the data analysis in the following chapter. Upon hydration, the time series of the temperatures at the center of the heating element and the ambient room were kept stable as shown in Figure 3(a). The soil temperatures were relatively stable during the hydration stage of this test as shown in Figures 3(b), 3(c), and 3(d), although a slight decrease was noted near the end of the test, likely due to an increase in heat loss associated with an increase in thermal conductivity of the bentonite during hydration, as will be discussed later. To better depict the time dependence of temperature over the long duration of the test while still being able to observe the major changes in thermo-hydraulic variables occurring in the early stages of the test this and other time series are plotted on a semi-logarithmic scale. All the sensors (except the thermal needle probes) were automatically scanned every 60 s for the first 24 hours and then every 600 s for the rest of the test. At the end of the hydration test, several small specimens at different axial and radial locations were sampled for determining gravimetric water content using an oven at 110°C for 48 hours.

Hydraulic conductivity determination for unsaturated bentonite

The instantaneous profile method was adopted in this study to determine the hydraulic conductivity of unsaturated soils during liquid water imbibition. This method involves a discretization of Darcy's law as follows (Olson and Daniel 1981):

$$K_{\mathrm{w},i} = \frac{\Delta V_{\mathrm{w},i}}{A_i \Delta t}\left[\frac{-1}{\left(\frac{dh}{dr}\right)_i}\right] \tag{1}$$

where $K_{\mathrm{w},i}$ is the hydraulic conductivity; $\Delta V_{w,i}$ is the volume of water that has passed a point i in the soil profile during a time interval Δt; A_i is the area defined by the perimeter of the circle multiplied by the height of the soil layer, at position i; r is the radial distance for the center of the specimen base; h is the total hydraulic head, equal to:

$$h = z + \frac{u_w}{\gamma_w} \tag{2}$$

where z is the height from the specimen's middle layer; γ_{w} is the unit weight of water; u_w is the (negative) water pressure in the soil, with units of kPa. It is assumed that the osmotic potential of the soil does not vary with water content, so it is not included in Eq. (2). Assuming the air pressure in the unsaturated soil is zero, the suction, equal to $\psi = (u_a - u_w)$, may be substituted for the water pressure, as follows:

$$h = z - \frac{\psi}{\gamma_w} \tag{3}$$

The suction can be converted from the relative humidity (measured by the relative humidity sensor) by Kelvin's law as follows:

$$\psi = -\rho_w \frac{R_g T}{M_w} ln(RH) \tag{4}$$

where ψ is (total) suction; ρ_{w} is the density of water (0.998 Mg/m^3 at 20°C); R_{g} is the universal molar gas constant (8.31432 J/mol•K); T is the absolute temperature in K; M_{w} is the relative molar mass of water molecules (18.016 g/mol); RH is the relative humidity. During hydration, the suction at the side boundary where water enters the

drainage layer is assumed to be zero (Wang et al. 2013).

The gradient term in Eq. (1) can be calculated at each point as follows:

$$i_i = -1 - \frac{1}{\gamma_w}\left(\frac{\psi_i - \psi_{i-1}}{r_{i-1} - r_i}\right) \quad (5)$$

where i = 0 at the side boundary of the soil, which is assumed at a constant suction value during infiltration. For radial inward infiltration, the position i increases with distance from the side boundary. The gradient is typically large during transient infiltration into compacted bentonite (i.e., with an initial suction typically greater than 10000 kPa). During a given time interval Δt and radial interval r_i, the volume of water inward flow from a given point can be obtained by integrating the water content profile, as follows:

$$\Delta V_{w,i}^{j} = \sum_{i=1}^{n}\left(\theta^{j} - \theta^{j-1}\right)(r_{i+1} - r_i)A_i \quad (6)$$

where j represents the current time step; n is the total number of points.

RESULTS

Time-series results

The soil temperature time histories in Figure 3 demonstrate that soil temperatures stay stable at the very beginning of hydration as there is a distance from the sensor location to the drainage layer and the hydraulic conductivity of compacted bentonite is extremely low. After several hours of hydration, the soil temperature begins to decrease because the inflowing water temperature is much lower than the soil temperature. The soil temperature close to the heating element always maintains a higher temperature than the soil further away from the heating element. The results in Figure 3(d) also reveal that there is appreciable upward heat transfer from the cylindrical heating element and that the soil near the outer boundary of the container increased in temperature during pre-heating and stabilized at approximately 28.7°C, or about 6.1°C above ambient room temperature before water inflow.

As the compacted bentonite layer absorbed water from the outer boundary of the tank it began to swell which tended to push the concrete cap upward. The external vertical load was adjusted using the hydraulic loading ram to restrain the bentonite and ensure that the volume/vertical strain was close to zero (Figure 4(a)). The average swelling pressure calculated by the loading cell is also plotted in Figure 4(a), which may be different from the swelling pressure in an oedometer as the bentonite hydrates concentrically inward toward the center of the container and not uniformly across the diameter. Nonetheless, the results in Figure 4(a) reveal that the swelling pressure develops quickly at the beginning of hydration and then turns stable in a sigmoid way in semi-logarithmic coordinates. A total of 9620 ml of water flowed into the soil layer and the average degree of saturation calculated by the volume of water inflow and the volume of soil layers is shown in Figure 4(b). Note that the final degree of saturation is less than one indicating the soil layers are not fully saturated due to the existence of the central heating element. This is another reason why the swelling pressure measured in Figure 4(a) is lower than that from previous swelling pressure tests on MX80 bentonite performed in oedometers (Villar 2005).

Time series of relative humidity and volumetric water content at different locations are shown in Figures 4(c) and 4(d), respectively. Results in the figures depicted that at the beginning of hydration, the measured relative humidity/volumetric water content for the soil far from the water infiltration boundary almost stays stable or shows a minor decrease as the existing pores water continues diffusing outward accompanied by the heat transfer from the heating element, while the inflow water did not reach the measure location. After hundred hours of hydration, the relative humidity/volumetric water content starts to increase gradually, as the wetting front is followed by gradual hydrating of the water. Compared with the soil temperature time series from these sensors in

Figure 3(c), the relative humidity/volumetric water content time series continues to increase even after the temperature at this location had stabilized, indicating that the water flow and heat transfer processes occurred at different rates.

Evolution of thermal behavior

The evolutions of thermal conductivity, volumetric heat capacity, and thermal diffusivity measured in the bentonite as a function of volumetric water content inferred from the dielectric sensors at similar radial locations are shown in Figures 5(a), 5(b) and 5(c). The results indicate that the thermal conductivity increases during hydration as the water content in soil increases. The thermal conductivity at a radial location of 185 mm from the heating element is higher than that at locations of 100 and 50 mm, as the water was infiltrated from the side boundary to the tank center and the relative humidity and degree of saturation closer to the side boundary are higher than those in the inner parts of the soil layer.

An increase in thermal conductivity was observed during the initial stage of hydration in which the volumetric water content at the three target locations didn't increase or in some case decreased due to the coupled effects of heating (Figure 4(d)). This increase in thermal conductivity could have occurred due to local changes in dry density during hydration. Specifically, during hydration the bentonite near the boundaries of the tank adsorbs water from the drainage layer (Figure 2(b)) and tends to swell, which may compress the soil in the center of the tank. Thus, the dry densities of the bentonite at the sensor locations may have increased even though on average the volume of the bentonite did not change. Several studies have shown that soil thermal conductivity increases with increasing dry density (Tang et al. 2008; Lu et al. 2020).

Spatial distributions of key variables

The distribution in soil temperature with radial distance from the heating element

is summarized in Figure 6(a). Stable soil temperatures were achieved prior to the initiation of hydration as reported by Lu and McCartney (2022), and the slight decrease in temperature did not have a major effect on the distribution in temperature within the soil layer. Although the temperature at the center of the soil layer is maintained at 200 °C, a sharp gradient in soil temperature with distance is observed close to the heater, after which a more gradual temperature gradient is observed. A similar drop in soil temperature near the heater was also observed in tests and simulations on MX80 bentonite pellets in the NAGRA section at Mont Terri underground research laboratory (Gens et al. 2020). This distribution could be attributed to axial heat loss as well as radiational spreading of heat as a function of distance from the heater. The sharp drop-off in temperature noted in this study is likely a result of the small diameter of the heater.

The isochrone distributions of suction and local degree of saturation with radial distance from the heating element are summarized in Figures 6(b) and 6(c). The local degrees of saturation were calculated from the volumetric water contents inferred from the dielectric sensors. The overall volume of the soil layer was held approximately constant during hydration. Results show that the saturation of the soil layer close to the side boundary increases significantly at the beginning of hydration follow by a decreased rate and then close to fully saturated, while the change for the soil layer close to the heating element is limited. The overall trend line follows a sigmoid shape. Meanwhile, the time required for the suction/saturation to stabilize is longer than the time required for the temperature to stabilize, confirming that the times required to reach steady-state distributions in the relative humidity/water content and temperature may be different depending on the coupling between the thermal and hydraulic properties of a given soil. In fact, it may be difficult for the water distribution to reach a stable condition during coupled heating and hydration although it may approach a

dynamic thermo-hydraulic equilibrium stage in a sealed space.

The gravimetric water contents of the soil layer at different axial and radial locations are plotted in Figure 7. The dots in the contour plot represent the measurement locations. The gravimetric water content increases with distance from the heating element significantly, while the height dependence of the water content valuable is also notable. The middle soil layers close to the heating element hold very low water contents as they surround the heating element with high temperature (Figures 3(b) and 6(a)), while the water contents at the top and bottom soil layers are much higher than that of middle soil layer as the soil temperature is a bit lower as the heating element was buried in the middle of the soil. Although most of the side boundary is saturated, the gravimetric water content of the very top side boundary is still lower than the middle and bottom side boundaries due to the influence of the gravity of water. In fact, the saturation of the very top layer of the soil at different radial locations is significantly lower than that of the bottom saturation of the very top layer, because the water was first infiltrated into the drainage layer from to holds located at the bottom of the tank.

The evolutions of the suction and degree of saturation profiles in Figures 6(b) and 6(c) indicate that the changes in suction and degree of saturation mainly occurred in the outer part of the compacted bentonite layer less than 200 mm, and the very top and bottom center of the soil layer, while in the inner part limited changes were identified. This agrees with the post-test water content distribution curve and saturation spatial distribution (Figure 7), where much more change occurred near the wetting end. On one hand, as noted by Delage et al. (1998) and Ye et al. (2009), this phenomenon could be explained by separating the liquid water transfer from the water vapor diffusion: in the zone near the wetting face, the water transfer involves mainly the liquid water; by contrast, water vapor diffusion prevails in the zone far from the wetting face. Column

infiltration tests performed by Delage et al. (1998) showed that at 50 mm beyond the wetting face, the water transfer was mainly governed by vapor diffusion. On the other hand, the soil close to the heating element already reached a vapor equilibrium before hydration, and the incoming vapor will be dissipated outward due to heat transfer. Similar phenomena were also noticed in the experiments and numerical simulations that were part of the THERESA project, including mock-up scale heating-hydration tests on MX80 bentonite and column heating tests on FEBEX bentonite with and without water infiltration (Gens and Zandarin 2009). This study found that the hydraulic behavior may be sensitive to constitutive laws that are not always easy to determine, such as the retention curve, relative permeability, and, in some cases, gas permeability.

The hydration stage in this study lasted more than 4000 hours. While longer than many laboratory tests, the hydration process in a geologic repository is expected to last much longer. Thus, this study only focuses on the short- and medium-term thermo-hydraulic response, which are critical to understand as significant movement/change of hydraulic and thermal parameters take place in these time periods.

ANALYSIS

Movement of wetting front

Significant changes in water distribution in the compacted bentonite occurred during hydration. The evolution of saturation in Figure 6(c) indicates that there were three stages of water flow, an initial stage, the main wetting stage, and a dynamic equilibrium stage. The initial stage corresponds to the initial degree of saturation of the soil layers before hydration and in the first several hours when seldom water arrived at target locations. The main wetting stage occurs in the middle term of hydration when the water inflow from the side boundary plays a dominant role, resulting in a notable inward movement of the wetting front. The dynamic equilibrium stage takes place after

the soil absorbs a certain amount of water with a significant decrease of suction, accompanied by the movement of the wetting front slowing down and then gradually stabilizing, where the soil water reaches a thermohydraulic equilibrium between the thermally-induced vapor transfer outward from the heater and the water infiltration inward from the outer boundary.

Evaluation of transient SWRC

To understand the transient water retention paths of the bentonite under coupled heating and hydration process, the transient SWRCs depicting the degree of saturation versus matric suction for three locations (50, 60 and 100 mm from the heating element) are shown in Figure 8(a). Each of these locations has a different temperature associated with the central heating process as shown in Figure 8(b). The data at these locations was calculated by the arithmetic mean value of the degree of saturation and matric suction measured at two adjacent locations. For example, the degree of saturation at a radial distance of 60 mm from the heating element was calculated from the dielectric sensor measurements 50 mm and 70 mm. At all three locations in Figure 8(a), the bentonite transitions from a drying path to a wetting path, each starting from different initial values of suction and degree of saturation associated with the preceding drying stage (Lu and McCartney 2022). As it takes time for the wetting front of liquid water to reach the central locations in the bentonite layer, all the locations were still initially following a drying path due to the outward diffusion of water vapor associated with central heating even though the beginning points of the paths correspond to the initiation of hydration from the outer radial boundary of the soil layer. When the wetting front of liquid water reaches the locations shown in Figure 8(a), the bentonite transitions to a wetting path where significant decreases in suction are observed. The transient drying-wetting paths measured at each location confirm that the bentonite can

experience significant hysteresis during the heating-hydration process.

While the SWRC of compacted bentonite at room temperature is usually represented using the SWRC model of van Genuchten (1980), this SWRC is not suitable for elevated temperatures. Lu (2016) proposed a SWRC model that considers water retention by both adsorption and capillarity which may aid in identifying different ways that temperature may affect water retention. The SWRC of Lu (2016) is given as follows:

$$\theta(\psi) = \theta_{\mathrm{a}}(\psi) + \theta_{\mathrm{c}}(\psi) \tag{7a}$$

$$\theta_{\mathrm{a}}(\psi) = \theta_{\mathrm{a,max}}\left\{1 - \left[\exp\left(\frac{\psi - \psi_{\mathrm{max}}}{\psi}\right)\right]^{M}\right\} \tag{7b}$$

$$\theta_{\mathrm{c}}(\psi) = \frac{1}{2}\left[1 - \mathrm{erf}\left(\sqrt{2}\frac{\psi - \psi_{\mathrm{c}}}{\psi_{\mathrm{c}}}\right)\right][\theta_{\mathrm{s}} - \theta_{\mathrm{a}}(\psi)][1 + (\alpha\psi)^{N}]^{1/N-1} \tag{7c}$$

where $\theta_{\mathrm{a}}(\psi)$ is the adsorptive volumetric water content, $\theta_{\mathrm{a}}(\psi)$ is the capillary volumetric water content, $\theta_{\mathrm{a,max}}$ is the adsorption capacity that denotes the maximum water content due to adsorption forces, ψ_{max} is the maximum matric suction, ψ_{c} is the mean cavitation suction, erf() is the error function, M is the adsorption strength, α is a parameter related either to the air entry value when plotting the primary SWRC drying path or the shape of the hydration path when plotting the SWRC wetting path SWRC, and N is the capillary pore-size distribution parameter. For a constant porosity corresponding to restrained bentonite, the volumetric water contents in Eq. 7 can be converted to the degree of saturation as $S = \theta/n$. The shape of the capillary portion of the SWRC of Lu (2016) is essentially the same as the SWRC of van Genuchten (1980). To account for temperature effects on water retention by capillarity, the SWRC model of Grant and Salehzadeh (1996) can be incorporated into the SWRC of Lu (2016) in place of the terms in the last bracket in Eq. 7c, as follows:

$$\theta_c(\psi) = \frac{1}{2}\left[1 - \mathrm{erf}\left(\sqrt{2}\frac{\psi - \psi_c}{\psi_c}\right)\right][\theta_s - \theta_a(\psi)]\left\{1 + \left[\alpha\psi\left(\frac{\beta + T_r}{\beta + T}\right)\right]^N\right\}^{1/N-1} \quad (8)$$

where β is a model parameter describing the temperature effects on the SWRC for a given soil type, and T_r and T are the reference temperature (293.15 K) and local (soil) temperature, respectively. While McCartney (2022) described adjustments to the SWRC of Lu (2016) to consider temperature effects on water retention due to adsorption, they are not show here for brevity.

The suction-saturation experimental curves in Figure 8(a) for different locations show a shift with elevated temperature, which are reflected in fitted nonisothermal SWRCs of Lu (2016). The wetting path curve for the location closest to the heating element (e.g., 50 mm, which has a high temperature as shown in Figure 8(b)) shows a gentle development compared with the curves for the locations further from the heating element with lower temperatures. In the low degree of saturation range, where adsorbed water plays a significant role, the curve at 50 mm from the heating element is lower than the curve at 60 mm from the heating element. Meanwhile, the highest matric suction that represents the suction when the soil is completely dry and can be captured by extending the SWRC to zero saturation (e.g., Lu 2016), for the soil located 50 mm from the heating element is also believed to be smaller than the soils located further from the heating element. These phenomena indicate that the water retention capacity of bentonite decreases with the increase of temperature at high suctions.

Evaluation of hydraulic conductivity

To quantify the movement of the wetting front, the hydraulic conductivity of the compacted bentonite can be analyzed based on the suction profiles, as the hydraulic gradients and water fluxes at each measurement section and time can be deduced. To be specific, based on the suction profiles (Figure 6(b)), the hydraulic gradients and

water fluxes at each measurement section and time can be deduced following the methods shown in Figure 9. The hydraulic gradients were calculated as the tangent of suction profiles as indicated in Figure 9(a) and the water fluxes were determined by integrating the difference in the volumetric water content profiles at a time interval Δt as indicated in Figure 9(b). During initial heating of the soil, Lu and McCartney (2022) found that outward water flow occurred due to thermal-induced water vapor diffusion. In the case of the hydration stage reported in this study, a hydraulic gradient forms due to inward liquid water flow from the outer boundary. A wetting front attributed to inward movement of liquid water from the outer boundary was observed during hydration, and it was assumed that inward vapor diffusion was negligible during this hydration process. This assumption is consistent with previous research on the hydraulic conductivity of compacted bentonite under elevated temperatures using the instantaneous profile method (e.g., Ye et al. 2012; Liu 2019).

The hydraulic gradients obtained at the three different radial sections L = 50, 60 and 100 mm (from the heating element) are plotted versus suctions in Figure 10, while the relationship between the calculated hydraulic conductivity values and suction at the three different sections are plotted in Figure 11. Note that, to determine the hydraulic gradient of the water at the location 100 mm from the heating element, estimation of the suction at the location nearby (e.g., 125 mm from the heating element) is conducted by considering the profile distribution trend (Figure 6(b)) and the SWRC trend (Figure 8(a)). Each point in Figures 11(a), 11(b), and 11(c) corresponds to a calculated hydraulic conductivity for time intervals of 200, 400, and 800 hours, respectively. At the three measurement sections having different temperatures, different relationships were obtained. The section closest to the heating element (e.g., 50 mm) has a higher temperature (Figure 10(b)) and also has a higher hydraulic gradient than sections further

from the heating element.

One possible interpretation is that the thermal contraction due to the heating element and the compression by the outer soil layer due to bentonite swelling upon hydrating led to a reduction of void ratio for the soil close to the heating element. Curves in Figure 11 show that the calculated hydraulic conductivity shows significant suction dependence as for the same temperature condition, lower suction shows higher hydraulic conductivity. This phenomenon is consistent with previous research, due to the further connection of the water channel.

By applying Darcy's law, relationships between the hydraulic gradient and suction, as well as the hydraulic conductivity and suction were obtained at different measurement sections (Figures 10 and 11). A linear relationship between the water flow rate and the hydraulic gradient is usually obtained when experimentally determining the hydraulic conductivity for sandy soils based on Darcy's law. However, non-linear relationships are often observed for clayey soils (Miller and Low 1963; Zou 1996), and there is a "critical gradient" below which flow occurs in non-Darcian conditions (Yong and Warkentin 1975; Dixon et al. 1987). In addition, higher temperature contributes to hydraulic conductivity, as the elevated temperature could reduce the viscosity of water to contribute to water flow and may cause bound water to flow.

To define the HCF, it was assumed that liquid water flow in bentonite primarily occurs within the water retention regime dominated by capillarity. Accordingly, the SWRC model of Grant and Salehzadeh (1996) was combined with the statistical model of Mualem (1976) to obtain the hydraulic conductivity function (HCF) from the SWRC parameters:

$$K_{\mathrm{w}}(T) = K_{\mathrm{sat}}(T)\frac{\left\{1 - \left[\alpha\psi\left(\frac{\beta + T_{\mathrm{r}}}{\beta + T}\right)\right]^{(N-1)} \cdot \left[1 + \left[\alpha\psi\left(\frac{\beta + T_{\mathrm{r}}}{\beta + T}\right)\right]^{N}\right]^{1/N-1}\right\}^{2}}{\left[1 + \left[\alpha\psi\left(\frac{\beta + T_{\mathrm{r}}}{\beta + T}\right)\right]^{N}\right]^{0.5(1-1/N)}} \tag{9}$$

where K_{sat} is the saturated hydraulic conductivity. The temperature effects on the saturated hydraulic conductivity can be expressed as follows:

$$K_{\mathrm{sat}}(T) = \frac{\kappa(T)\,\rho_{\mathrm{w}}(T)g}{\eta(T)} \tag{10}$$

where κ is the intrinsic hydraulic conductivity of soil; ρ_{w} is the density of water; g is the acceleration of gravity; η is water viscosity. The water viscosity and liquid water density will vary with temperature as follows:

$$\eta(T) = A10^{B(T-C)^{-1}} \tag{11}$$

$$\rho_{\mathrm{w}}(T) = \frac{1}{1 + 0.0002(T - 293.15)} \tag{12}$$

where T is the absolute temperature in K, and A, B, and C are fitting parameters with values of 0.0000242, 247.8, and 140, respectively, obtained by fitting Eq. (11) to measured data of Fox et al. (2003). The change of water viscosity plays a dominant role as it is most sensitive to temperature, while the change in water density with temperature is relatively small.

Most studies assume the intrinsic hydraulic conductivity is independent of temperature and is only related to the mineralogical properties of the soil and the void ratio. However, heating of bentonite may cause movement of high-density adsorbed water to the macro (inter-aggregate) pores where it becomes free water (Villar and Lloret 2004). Under constant-volume conditions, heating may cause an increase in the proportion of free water in the porous channels (inter-aggregate) and the available area for water flow. To account for this phenomenon, Cho et al. (1999) found that the intrinsic hydraulic conductivity and temperature follows a log-linear relationship, as

follows:

$$\kappa(T) = \exp[A' + B'(T - 273.15)] \tag{13}$$

where A' and B' are fitting parameters that consider the thermo-physical properties of a soil governing its impedance to water flow. The parameters for MX80 bentonite compacted to a dry density of 1.305 Mg/m^3 were estimated to be A' = −43.858 and B' = 0.0095 based on hydraulic conductivity results in the literature (Villar 2005).

An expression for the nonisothermal saturated hydraulic conductivity of bentonite can be obtained by substituting Eqs. (11), (12) and (13) into Eq. (10) as follows:

$$K_{\text{sat}}(T) = \frac{\exp[A' + B(T - 273.15)]g}{[1 + 0.0002(T - 293.15)]\left[A10^{B(T-C)^{-1}}\right]} \tag{14}$$

Using this equation, the values of saturated hydraulic conductivity at different temperatures and different radial sections can be estimated. For the three different sections (50, 60 and 100 mm from the heating element) with different temperatures, the evolution of the hydraulic conductivity of unsaturated bentonite for each location was fitted using Eq. (9) considering the nonisothermal saturated hydraulic conductivity as shown in Figure 11. The HCFs defined with model parameters (α, β and N) from the SWRC fitting in Figure 8(a) represent the experimental hydraulic conductivity and suction data well. The downward shift in the HCF with temperature is mainly controlled by the decrease in saturated hydraulic conductivity with increasing temperature. Only slight effects associated with the effect of temperature on the water retention by capillarity from the equation of Grant and Salehzadeh (1996). The effect of temperature on the HCF diminishes with increasing suction. The HCFs in Figures 11(a), 11(b), and 11(c) correspond well with the hydraulic conductivity values defined at different time intervals, indicating that the instantaneous profile method provides a reliable estimate of hydraulic conductivity values for bentonite during hydration.

Analysis of thermal conductivity data

Lu and McCartney (2023) proposed a closed-form equation for the thermal conductivity of unsaturated soils, given as follows:

$$\frac{\lambda - \lambda_{\text{dry}}}{\lambda_{\text{sat}} - \lambda_{\text{dry}}} = \left[1 - \frac{1 - S^m}{1 + \left(\frac{S}{S_c}\right)^m}\right]^{1-1/m} \tag{15}$$

where λ is thermal conductivity; λ_{dry} and λ_{sat} are the thermal conductivities for the dry and saturated soil, corresponding to the minimum and the maximum thermal conductivity, respectively; S is the degree of saturation; S_c is the degree of saturation at the onset of the capillary water retention regime, and m is a model parameter that reflects the changing rate of the thermal conductivity with the degree of saturation. The latter parameter reflects the connection of pore water network connectivity among soil particles and is related to the pore-size parameter n in the SWRC model. Eq. (15) has been fitted to thermal conductivity data of different unsaturated sandy and clayey soils and can capture trends in thermal conductivity well in both the low and high degree of saturation ranges. A comparison of the measured thermal conductivity in this work and the fitted TCF of Lu and McCartney (2023) is shown in Figure 12. The TCF model of Lu and McCartney (2023) captures the shape of the thermal conductivity versus degree of saturation of the compacted MX80 bentonite well. Regardless of the temperature at the different radial locations, there is not a significant temperature dependency on the evolution in thermal conductivity, confirming that the TCF does not depend on temperature like the SWRC and HCF. However, the nonlinear shape of the thermal conductivity data at the initiation of hydration differs from the shape of the fitted TCF, possibly due to local volume changes in the bentonite during transient hydration from the outside of the container toward the center.

CONCLUSIONS

This paper presents results from a tank-scale test to investigate the coupled thermo-hydraulic response of a MX80 bentonite layer during water imbibition under an elevated central heater temperature of 200 °C. The steep thermal gradient associated with coupled radial heat transfer and hydration represents the axisymmetric conditions in a geological repository, providing a benchmark for numerical simulation on the long-term behavior of barrier systems, and novel insights were gained from the evaluation of the transient wetting front through the bentonite layer into the effects of temperature on the transient SWRC, HCF, and TCF. Interpretation of data from embedded sensors in the bentonite layer was useful to confirm the functional forms of the temperature-dependent thermo-hydraulic properties. The following specific conclusions can be drawn from the analysis of the experimental results:

1) The time required for the suction and degree of saturation to stabilize is longer than the time required for the temperature to stabilize, confirming that the times required to reach steady-state distributions in relative humidity, volumetric water content and temperature may be different depending on the coupling between the thermo-hydraulic properties of the bentonite. The wetting stage occurs when the liquid water inflow from the side boundary results in a notable inward movement of the wetting front, followed by a dynamic equilibrium stage where the soil-water reaches a thermo-hydraulic equilibrium between the thermally-induced vapor flow outward from the heater and water infiltration inward from the outer boundary.

2) The transient relationships between degree of saturation and suction measured at locations with different temperatures all initially follow a drying path associated with ongoing outward diffusion of water vapor due to central heating, but then transitions to a wetting path when the liquid water wetting front reaches these locations. Fitted

SWRCs confirm a shift in water retention with elevated temperature, with the water retention capacity of bentonite decreasing with the increase of temperature at a given suction. The wetting front during imbibition was primarily in the capillary regime.

3) A nonisothermal HCF developed for compacted bentonite was found to have a good match with experimental hydraulic conductivity values at different degrees of saturation and temperatures obtained from the instantaneous profile method. The nonisothermal HCF for liquid water flow in bentonite was found to be linked to the regime of the SWRC dominated by capillarity following the model of Mualem (1976). This is important when predicting the HCF from advanced SWRCs like that of Lu (2016) that consider water retention by both capillarity and adsorption mechanisms. While temperature effects on the water retention by capillarity were considered in the HCF, they were found not to have a major effect on the shape of the HCF. The effects of temperature on the hydraulic conductivity in saturated conditions played a greater role in the changes in the HCF with temperature.

4) The thermal conductivity measured in the tank-scale test was found to follow the nonlinear shape of a newly proposed isothermal TCF for the bentonite during hydration. The thermal conductivity at locations having different temperatures followed the same relationship, confirming that the TCF is not sensitive to temperature.

Overall, this study provided a new understanding of the linkages between the SWRC, HCF, and TCF for compacted granular bentonite under high temperature gradients, albeit under a lower dry density compared to that used in actual repositories. These observations on the thermo-hydraulic properties of compacted bentonite during hydration under elevated temperature will be useful for simulating coupled heat transfer and water flow processes in hydrogeologic and geotechnical applications, which can be critical for long-term simulations of buffer systems in nuclear waste repositories. Future

experimental studies with advanced sensors (e.g., wireless transmission, smaller size, etc.) may be necessary to understand the THM behavior of bentonite under higher compaction efforts different bentonite-based materials (e.g., bentonite pellets, bentonite-sand mixtures), which may have different size and boundary effects than considered in this study.

ACKNOWLEDGEMENTS

The authors appreciate support from US Department of Energy Nuclear Energy University Program award DE-NE008951. The views in this paper are those of the authors alone.

REFERENCES

Abed, A.A., and Sołowski, W.T. 2017. A study on how to couple thermo-hydro-mechanical behaviour of unsaturated soils: Physical equations, numerical implementation and examples. Computers and Geotechnics, **92**: 132–155.

Abootalebi, P., and Siemens, G. 2018. Thermal properties of engineered barriers for a Canadian deep geological repository. Canadian Geotechnical Journal, **55**(6): 759–776.

Börgesson, L., Fredrikson, A., and Johannesson, L.E. 1994. Heat conductivity of buffer materials. Swedish Nuclear Fuel and Waste Management Co.

Boynton, S.S., and Daniel, D.E. 1985. Hydraulic conductivity tests on compacted clay. Journal of Geotechnical Engineering, **111**(4): 465–478.

Cho, W.J., Lee, J.O., and Chun, K.S. 1999. The temperature effects on hydraulic conductivity of compacted bentonite. Applied Clay Science, **14**(1–3): 47–58.

Cui, Y.J., Tang, A.M., Loiseau, C., and Delage, P. 2008. Determining the unsaturated hydraulic conductivity of a compacted sand-bentonite mixture under constant-volume and free-swell conditions. Physics and Chemistry of the Earth, Parts

A/B/C, **33**(S1): S462–S471.

Dai, Z., Samper, J., Wolfsberg, A., and Levitt, D. 2008. Identification of relative conductivity models for water flow and solute transport in unsaturated bentonite. Physics and Chemistry of the Earth, Parts A/B/C, **33**: S177–S185.

Delage, P., Cui, Y.J., Yahia-Aissa, M., and De Laure, E. 1998. On the unsaturated hydraulic conductivity of a dense compacted bentonite. Proceedings of the second International Conference on Unsaturated Soils, 27–30 August, Beijing, China, vol. 1, pp. 344–349.

Dixon, D.A., Cheung, S.C.H., Gray, M.N., and Davidson, B.C. 1987. The hydraulic conductivity of dense clay soils. Proceedings of 40th Canadian Geotechnical Conference, Regina, Saskatchewan, Canada, pp. 389–396.

Dixon, D.A., Graham, J., and Gray, M.N. 1999. Hydraulic conductivity of clays in confined tests under low hydraulic gradients. Canadian Geotechnical Journal, **36**(5): 815–825.

Dixon, D., Stone, J., Birch, K., and Kim, C.S. 2023. Sealing materials for a deep geological repository: Evaluation of swelling pressure and hydraulic conductivity data for bentonite-based sealing materials proposed for use in placement rooms. Canadian Geotechnical Journal, online. https://doi.org/10.1139/cgj-2021-0609.

Dong, Y., McCartney, J.S., and Lu, N. 2015. Critical review of thermal conductivity models for unsaturated soils. Geotechnical and Geological Engineering, **33**(2): 207–221.

Dudoignon, P., Gélard, D., and Sammartino, S. 2004. Cam-clay and hydraulic conductivity diagram relations in consolidated and sheared clay-matrices. Clay Minerals, **39**(3): 267–279.

Fox, R.W., McDonald, A.T., and Pritchard, P.J. 2003. Introduction to Fluid Mechanics.

(6Ed) John Wiley and Sons, Hoboken.

Grant, S.A., and Salehzadeh, A. 1996. Calculation of temperature effects on wetting coefficients of porous solids and their capillary pressure functions. Water Resources Research, **32**(2): 261–270.

Gens, A., Alcoverro, J., Blaheta, R., Hasal, M., Michalec, Z., Takayama, Y., Lee, C., Lee., J., Kim, G.Y., Kuo, C.W., Kuo, W.J., Lin, C.Y. 2021. HM and THM interactions in bentonite engineered barriers for nuclear waste disposal. International Journal of Rock Mechanics and Mining Sciences, **137**: 104572.

Gens, A., de Vasconcelos, R.B., and Olivella, S. 2020. Towards higher temperatures in nuclear waste repositories. E3S Web of Conferences Vol. **205**, No. 01001, pp. 1-8. EDP Sciences.

Gens, A., and Zandarin, M.T. 2009. Capabilities and requirements of numerical models. THERESA. Deliverable 11.

Grimsel Test Site (GTS). 2022. HotBENT Introduction. http://web.archive.org/web/20220525182521/https://grimsel.com/gts-projects/hotbent-high-temperature-effects-on-bentonite-buffers/hotbent-introduction, Accessed on 10/14/2022.

Ito, D., Wang, H., and Komine, H. 2022. Hydraulic conductivity test system for compacted, 2-mm-thick bentonite specimens. Soils and Foundations, **62**(5): 101210.

Johnson, L.H., Tait, J.C., Shoesmith, D.W., Crosthwaite, J.L., and Gray, M.N. 1994. The disposal of Canada's nuclear fuel waste: engineered barriers alternatives (No. AECL-10718). Atomic Energy of Canada Limited.

Kim, C.S., and Dixon, D. 2013. Evaluating hydro-mechanical interactions of adjacent clay-based sealing materials. Physics and Chemistry of the Earth, Parts A/B/C, **65**: 98–110.

Kim, C.S., Alfaro, M.C., Blatz, J., and Graham, J. 2019. Coupled hydromechanical (HM) performance of in situ shaft sealing components for nuclear waste disposal. Canadian Geotechnical Journal, **56**(11): 1638–1649.

Kim, C.S., Alfaro, M.C., Blatz, J., and Graham, J. 2020. Swelling pressures and hydration times in a clay seal. Environmental Geotechnics, **9**(5): 298–309.

Komine, H., and Ogata., N. 1994. Experimental study on swelling characteristics of compacted bentonites. Canadian Geotechnical Journal, **31**(4): 478–490.

Kröhn, K.P. 2003. New conceptual models for the resaturation of bentonite. Applied Clay Science, **23**(1–4): 25–33.

Liu, Z.R. 2019. Investigation on the packing behaviour and thermal-hydraulic properties of GMZ bentonite pellet mixtures. Ph.D. Thesis, Tongji University, Shanghai.

Lloret, A., Villar, M.V., Sánchez, M., Gens, A., Pintado, X., and Alonso, E.E. 2003. Mechanical behaviour of heavily compacted bentonite under high suction changes. Geotechnique, **53**(1): 27–40.

Lu, N., and Dong, Y. 2015. Closed-form equation for thermal conductivity of unsaturated soils at room temperature. Journal of Geotechnical and Geoenvironmental Engineering, **141**(6), 04015016.

Lu, N. 2016. Generalized soil water retention equation for adsorption and capillarity. Journal of Geotechnical and Geoenvironmental Engineering, **142**(10): 04016051.

Lu, Y., Ye, W.M., Wang, Q., Zhu, Y.H., Chen, Y.G., and Chen, B. 2020. Investigation on anisotropic thermal conductivity of compacted GMZ bentonite. Bulletin of Engineering Geology and the Environment, **79**(3): 1153–1162.

Lu, Y., Ye, W.M., Wang, Q., Zhu, Y.H., Chen, Y.G., and Chen, B. 2021. Anisotropic swelling behaviour of unsaturated compacted GMZ bentonite hydrated under

vertical stresses. Bulletin of Engineering Geology and the Environment, **80**(7): 5515–5526.

Lu, Y., and McCartney, J.S. 2022. Physical modeling of coupled thermohydraulic behavior of compacted MX80 bentonite during heating. Geotechnical Testing Journal, **45**(6): 20220054

Lu, Y., and McCartney, J.S. 2023. Thermal conductivity function for fine-grained unsaturated soils linked with water retention by capillarity and adsorption. Journal of Geotechnical and Geoenvironmental Engineering, In review.

Marcial, D., Delage, P., and Cui, Y.J. 2002. On the high stress compression of bentonites. Canadian Geotechnical Journal, **39**(4): 812–820.

Mualem, Y. 1976. A new model for predicting the hydraulic conductivity of unsaturated porous media. Water Resources Research. **12**(3): 513-522.

Olson, R.E., and Daniel, D.E. 1981. Measurement of the hydraulic conductivity of fine-grained soils. Permeability and Groundwater Contaminant Transport, ASTM STP, **746**: 18–64.

Pusch. R. 1979. Highly Compacted sodium bentonite for isolating rock-deposited radioactive waste products. Nuclear Technology, **45**(2): 153–157.

Pusch, R. 1980. Permeability of highly compacted bentonite. Swedish Nuclear Fuel and Waste Management Company. Technical Report 80-16.

Schanz, T., and Al-Badran, Y. 2014. Swelling pressure characteristics of compacted Chinese Gaomiaozi bentonite GMZ01. Soils and Foundations, **54**(4): 748–759.

Svemar, C., and Pusch, R. 2000. Äspö Hard Rock Laboratory. Prototype Repository. Project description. FIKW-CT-2000-00055. International Progress Report IPR-00-30. Svensk Kärnbränslehantering AB (SKB), Stockholm.

Tang, A.M., Cui, Y.J. and Le, T.T. 2008. A study on the thermal conductivity of

compacted bentonites. Applied Clay Science, **41**(3–4): 181–189.

Thomas, H.R., Siddiqua, S., and Seetharam, S.C. 2009. Inclusion of higher-temperature effects in a soil behaviour model. Géotechnique, **59**(3): 279–282.

Thomas, H.R., Vardon, P.J., and Cleall, P.J. 2014. Three-dimensional behaviour of a prototype radioactive waste repository in fractured granitic rock. Canadian Geotechnical Journal, **51**(3): 246–259.

van Genuchten, M.T. 1980. A closed-form equation for predicting the hydraulic conductivity of unsaturated soils. Soil Science Society of America Journal, **44**(5): 892–898.

Vardon, P.J. 2009. A three-dimensional numerical investigation of the thermo-hydro-mechanical behaviour of a large-scale prototype repository. Ph.D. Thesis, Cardiff University, Cardiff.

Villar, M.V. 2005. MX-80 Bentonite. Thermal-Hydro-Mechanical characterisation performed at CIEMAT in the context of the prototype project. CIEMAT-1053. Spain.

Villar, M.V., and Gomez-Espina, R. 2009. Report on thermo-hydro-mechanical laboratory tests performed by CIEMAT on FEBEX bentonite 2004-2008 (No. CIEMAT-1178). Centro de Investigaciones Energeticas Medioambientales y Tecnologicas (CIEMAT).

Villar, M.V., and Lloret, A. 2004. Influence of temperature on the hydromechanical behaviour of a compacted bentonite. Applied Clay Science, **26**: 337–350.

Villar, M.V., Martın, P.L., Gómez-Espina, R., Romero, F.J., and Barcala, J.M. 2012. Long-term THM tests reports: THM cells for the HE-E test: setup and first results. PEBS report D2.2-7.1, CIEMAT technical report CIEMAT/DMA/2G210/02/2012.

Villar, M.V., Martín, P.L., and Romero, F.J. 2014. Long-term THM tests reports: THM cells for the HE-E test: update of results until February 2014. PEBS: D2.2-7.3,

CIEMAT Technical Report IEMAT/DMA/2G210/03/2014.

Watanabe, Y., Yokoyama, S., Shimbashi, M., Yamamoto, Y., and Goto, T. 2023. Saturated hydraulic conductivity of compacted bentonite–sand mixtures before and after gas migration in artificial seawater. Journal of Rock Mechanics and Geotechnical Engineering, **15**(1): 216–226.

Watson, K. 1966. An instantaneous profile method for determining the hydraulic conductivity of unsaturated porous materials. Water Resources Research, **2**(4): 709–715.

Wang, Q., Cui, Y.J., Tang, A.M., Barnichon, J.D., Saba, S., and Ye, W.M. 2013. Hydraulic conductivity and microstructure changes of compacted bentonite/sand mixture during hydration. Engineering Geology, **164**: 67–76.

Ye, W.M., Cui, Y.J., Qian, L.X., and Chen, B. 2009. An experimental study of the water transfer through confined compacted GMZ bentonite. Engineering Geology, **108**(3–4): 169–176.

Ye, W.M., Wan, M., Chen, B., Chen, Y.G., Cui, Y.J. and Wang, J. 2012. Temperature effects on the unsaturated permeability of the densely compacted GMZ01 bentonite under confined conditions. Engineering Geology, **126**: 1–7.

Ye, W.M., Borrell, N.C., Zhu, J.Y., Chen, B., and Chen, Y.G. 2014. Advances on the investigation of the hydraulic behavior of compacted GMZ bentonite. Engineering Geology, **169**: 41–49.

Yong, R.N., and Warkentin, B.P. 1975. Soil Properties and Behaviour. Elsevier, Amsterdam.

Zeng, Z., Cui, Y.J., and Talandier, J. 2022. Investigation of the hydraulic conductivity of an unsaturated compacted bentonite/claystone mixture. Géotechnique, **72**(10): 911–921.

Zheng, L.G., Rutqvist, J., Birkholzer, J.T. and Liu, H.H. 2015. On the impact of temperatures up to 200 °C in clay repositories with bentonite engineer barrier systems: A study with coupled thermal, hydrological, chemical, and mechanical modeling. Engineering Geology, **197**: 278–295.

Zheng, L.G, Rutqvist, J., Xu, H., and Birkholzer, J.T. 2017. Coupled THMC models for bentonite in an argillite repository for nuclear waste: Illitization and its effect on swelling stress under high temperature. Engineering Geology, **230**: 118–129.

Zou, Y. 1996. A non-linear permeability relation depending on the activation energy of pore liquid. Geotechnique, **46**(4): 769–774.

TABLES

Table 1. Initial conditions of the MX80 bentonite layer before heating (after compaction) and after heating (prior to hydration)

Parameter	Before heating	Before hydration
Thickness (mm)	210.5	211.0
Total density (Mg/m^3)	1.472	1.469
Dry density (Mg/m^3)	1.308	1.305
Gravimetric water content (%)	12.55	12.55
Volumetric water content (m^3/m^3)	0.164	0.164
Void ratio (m^3/m^3)	1.034	1.038
Porosity (m^3/m^3)	0.508	0.509
Degree of saturation (m^3/m^3)	0.323	0.322

Note: “Before heating” represents the very initial stage when the soil layers were compacted at ambient room conditions; “Before hydration” represents the initial stage in this work where a pre-heating process has been conducted and the soil temperatures were stable.

LIST OF FIGURE CAPTIONS

Figure 1. Summary of coupled heat transfer and water flow processes in a bentonite buffer

Figure 2. Tank test setup: (a) Picture of the assembled experimental setup; (b) Schematic cross-section showing instrumentation locations

Figure 3. Evolution of temperatures: (a) Central heating element and ambient room; (b) Inside the layer obtained from relative humidity sensors; (c) Inside the layer obtained from dielectric sensors; (d) At the top-center and side boundary of the layer obtained from thermocouples

Figure 4. Time series of the hydro-mechanical response of the soil layer at different locations during hydration: (a) Vertical strain and swelling pressure; (b) Average degree of saturation; (c) Relative humidity; (d) Volumetric water content

Figure 5. Evolution of soil thermal responses versus volumetric water content: (a) Thermal conductivity; (b) Volumetric heat capacity; (c) Thermal diffusivity

Figure 6. Radial profile plots of thermo-hydraulic variables at different times during heating: (a) Temperature; (b) Suction; (c) Local degree of saturation

Figure 7. Gravimetric water content and local degree of saturation at different locations after hydration: (a) Gravimetric water content; (b) Local degree of saturation

Figure 8. Transient thermo-hydraulic responses at different locations in the soil layer: (a) Suction-saturation curves with drying and wetting path SWRCs; (b) Temperature-saturation curves

Figure 9. Determination of hydraulic gradient and water flux between two hydration times (e.g., 1000 and 1500 h): (a) Hydraulic gradient; (b) Water flux

Figure 10. Hydraulic gradient and corresponding temperature versus suction at different sections: (a) Hydraulic gradient; (b) Temperature

Figure 11. Hydraulic conductivity versus suction data and fitted HCFs for different radial sections having different average temperatures: (a) 200 h interval; (b) 400 h interval; (c) 800 h interval

Figure 12. Comparison of measured thermal conductivity at different radial locations and fitted TCF of Lu and McCartney (2023)

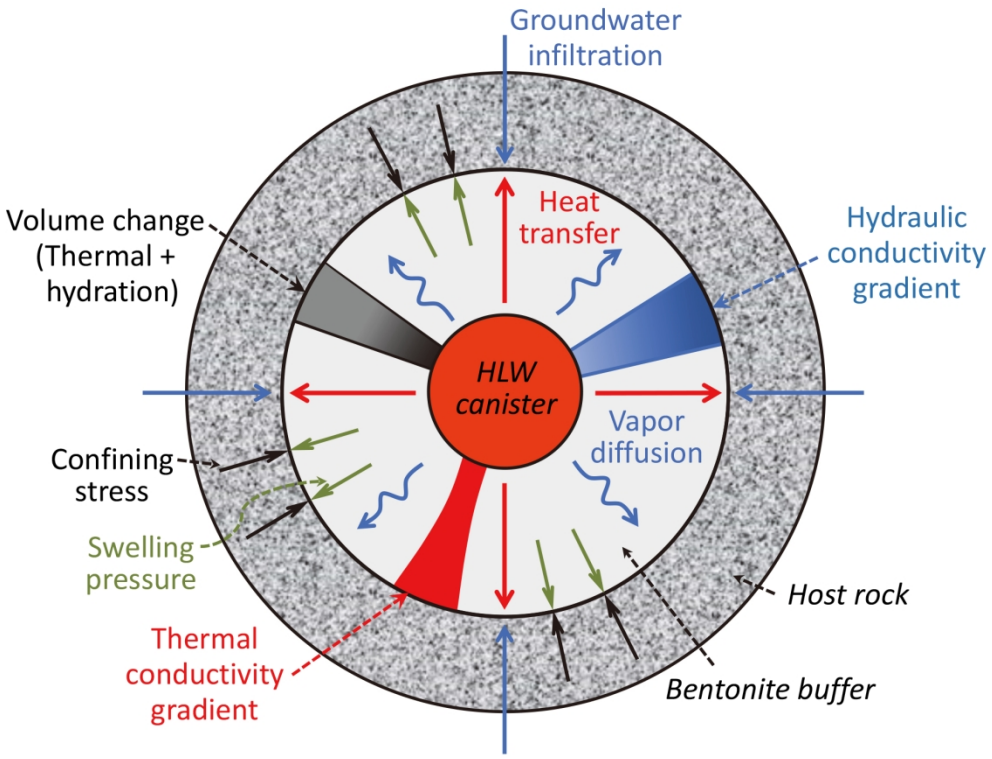

Figure 1. Summary of coupled heat transfer and water flow processes in a bentonite buffer

88x67mm (553 x 553 DPI)

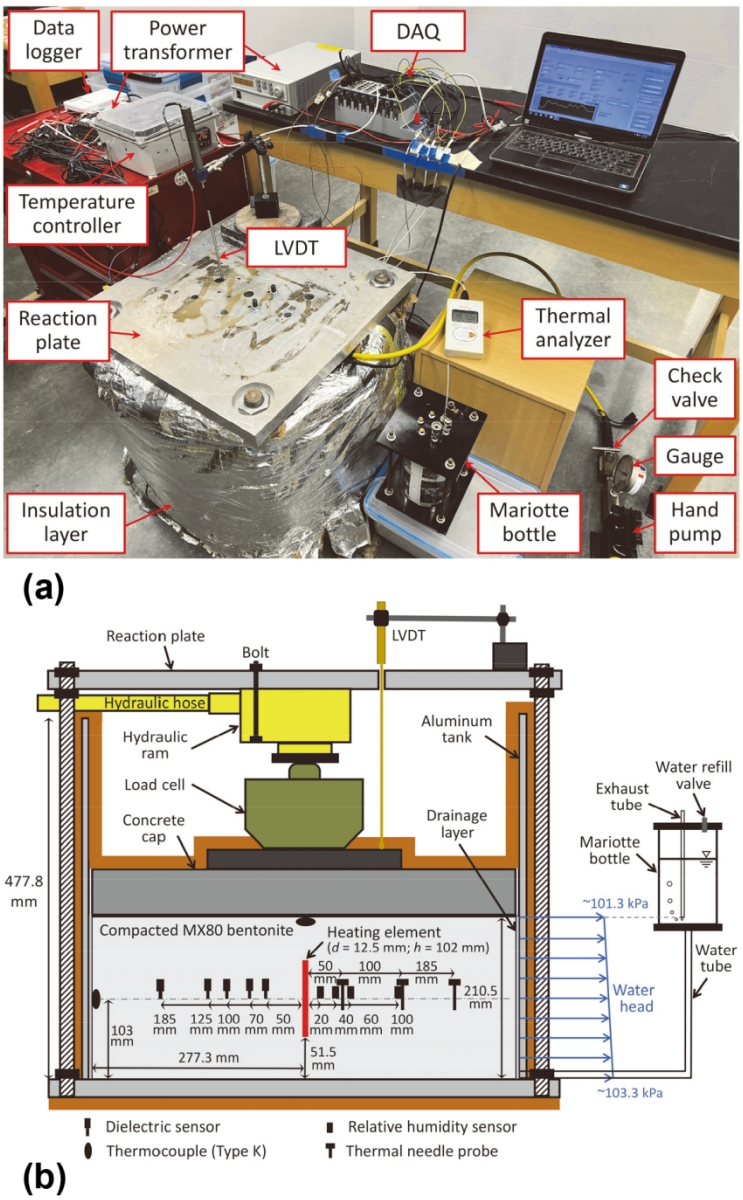

Figure 2. Tank test setup: (a) Picture of the assembled experimental setup; (b) Schematic cross-section showing instrumentation locations

88x144mm (330 x 330 DPI)

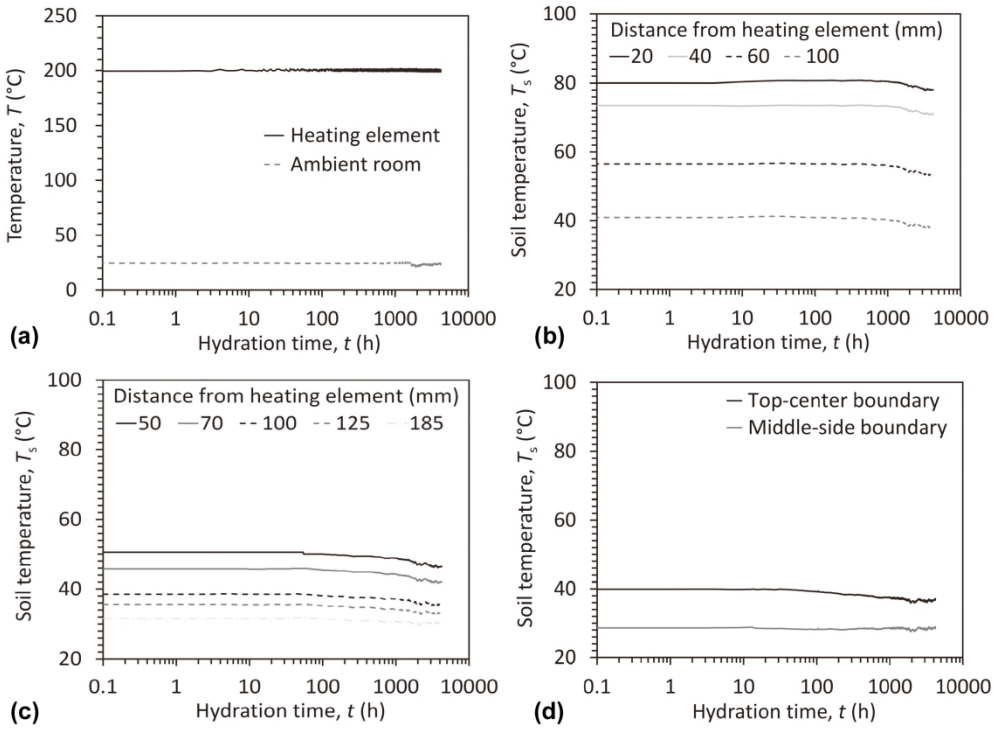

Figure 3. Evolution of temperatures: (a) Central heating element and ambient room; (b) Inside the layer obtained from relative humidity sensors; (c) Inside the layer obtained from dielectric sensors; (d) At the top-center and side boundary of the layer obtained from thermocouples

177x130mm (362 x 362 DPI)

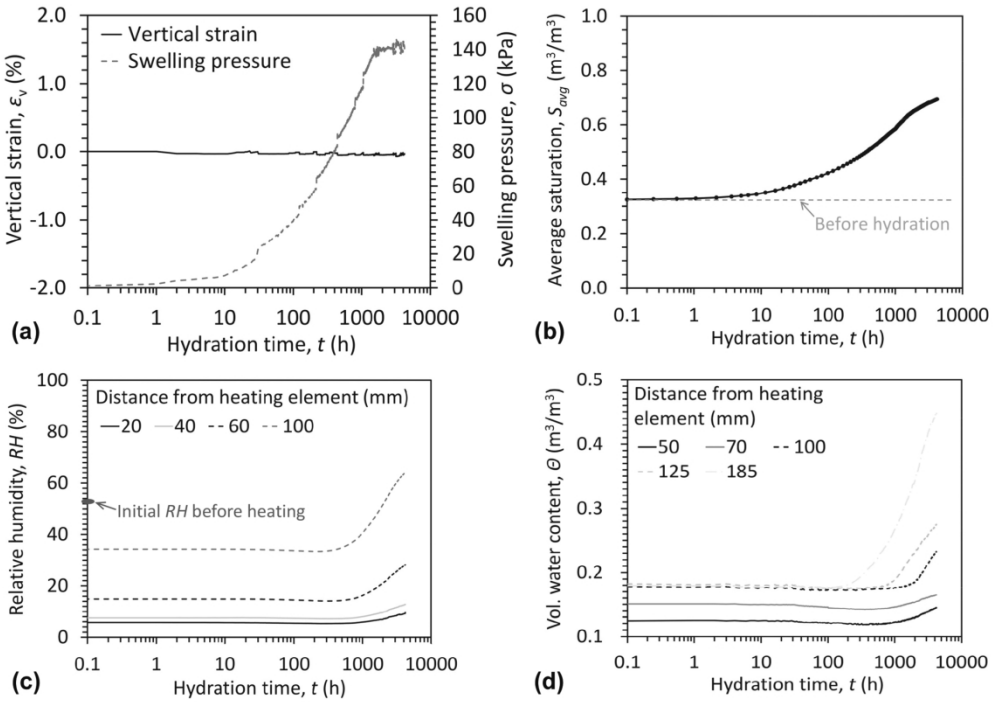

Figure 4. Time series of the hydro-mechanical response of the soil layer at different locations during hydration: (a) Vertical strain and swelling pressure; (b) Average degree of saturation; (c) Relative humidity; (d) Volumetric water content

177x127mm (300 x 300 DPI)

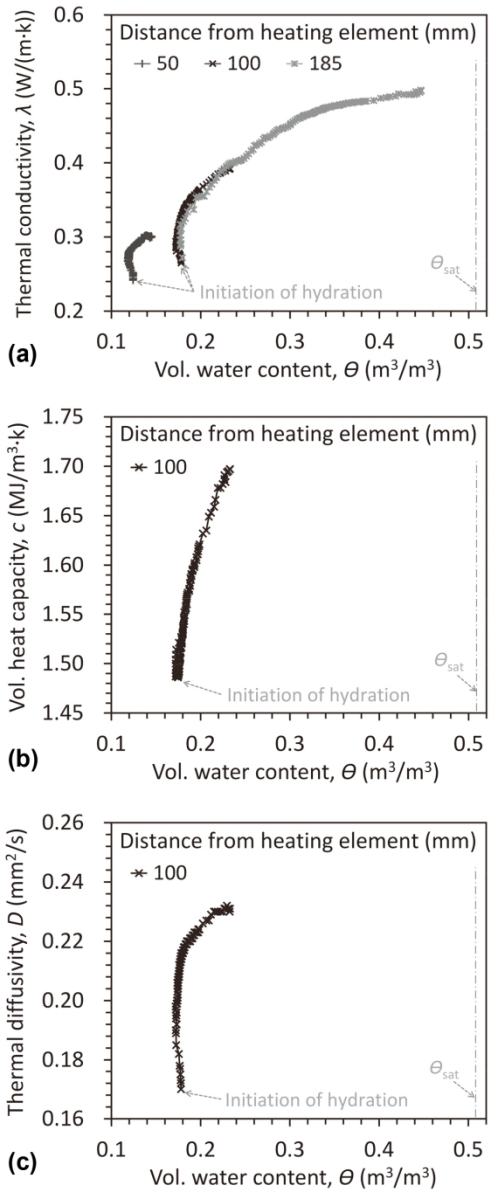

Figure 5. Evolution of soil thermal responses versus volumetric water content: (a) Thermal conductivity; (b) Volumetric heat capacity; (c) Thermal diffusivity

88x208mm (330 x 330 DPI)

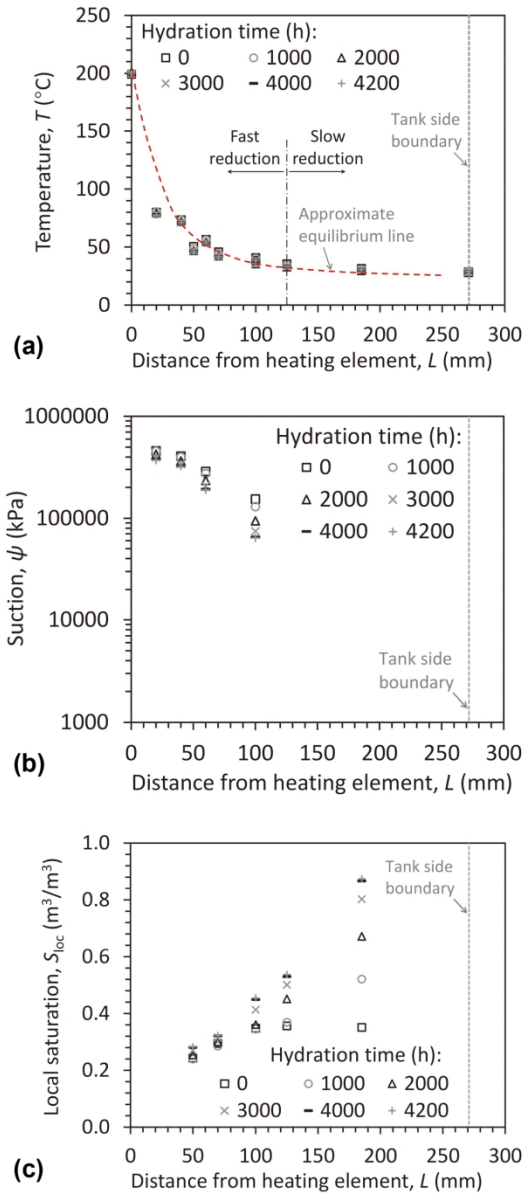

Figure 6. Radial profile plots of thermo-hydraulic variables at different times during heating: (a) Temperature; (b) Suction; (c) Local degree of saturation

88x201mm (330 x 330 DPI)

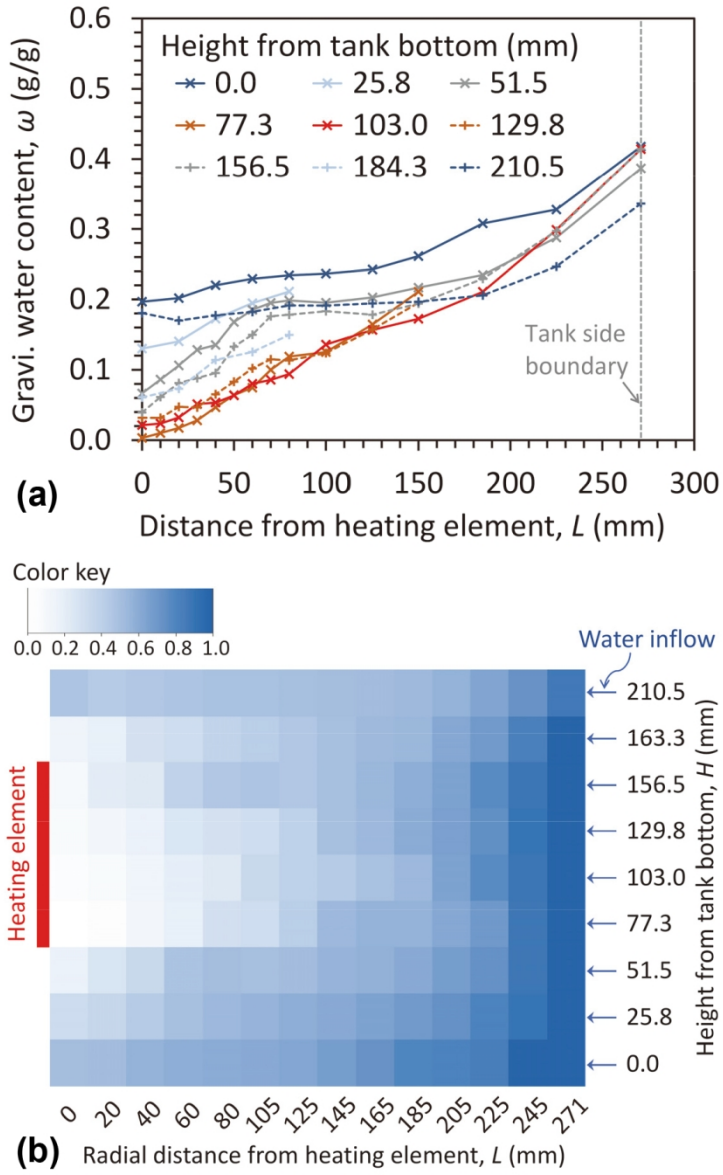

Figure 7. Gravimetric water content and local degree of saturation at different locations after hydration: (a) Gravimetric water content; (b) Local degree of saturation

88x145mm (330 x 330 DPI)

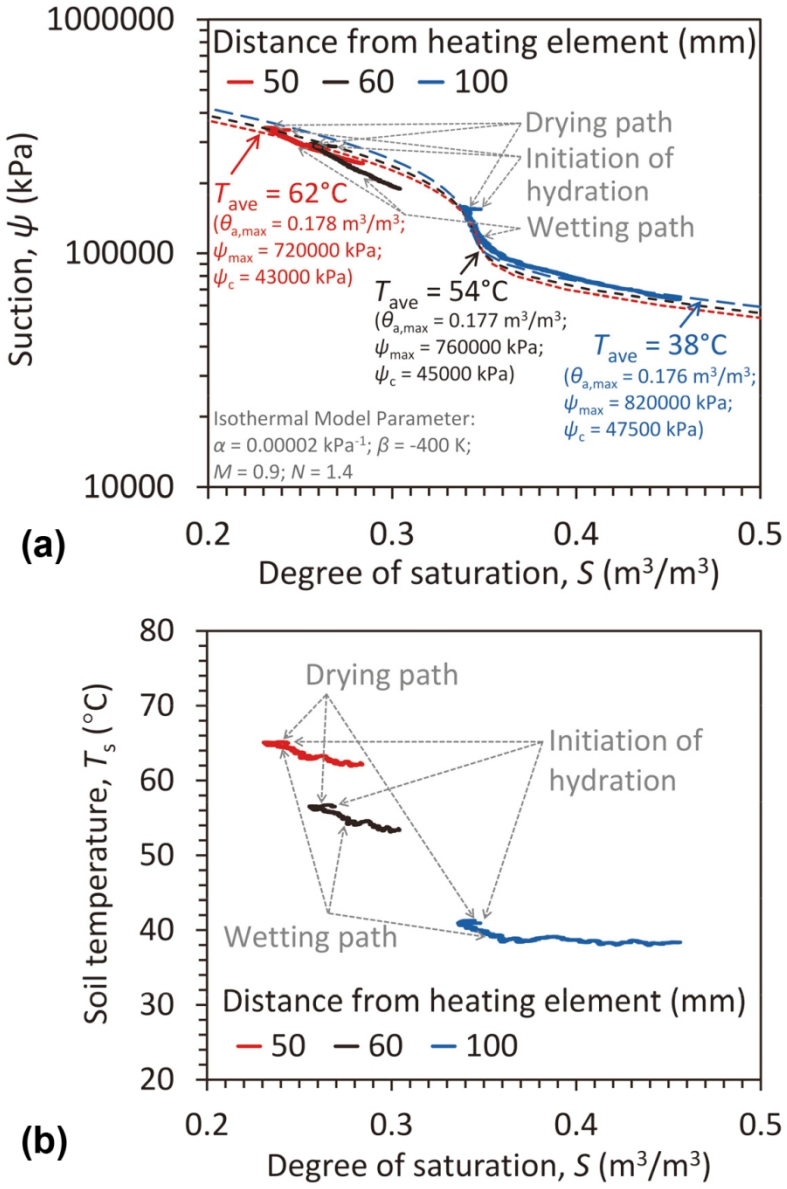

Figure 8. Transient thermo-hydraulic responses at different locations in the soil layer: (a) Suction-saturation curves with drying and wetting path SWRCs; (b) Temperature-saturation curves

88x135mm (330 x 330 DPI)

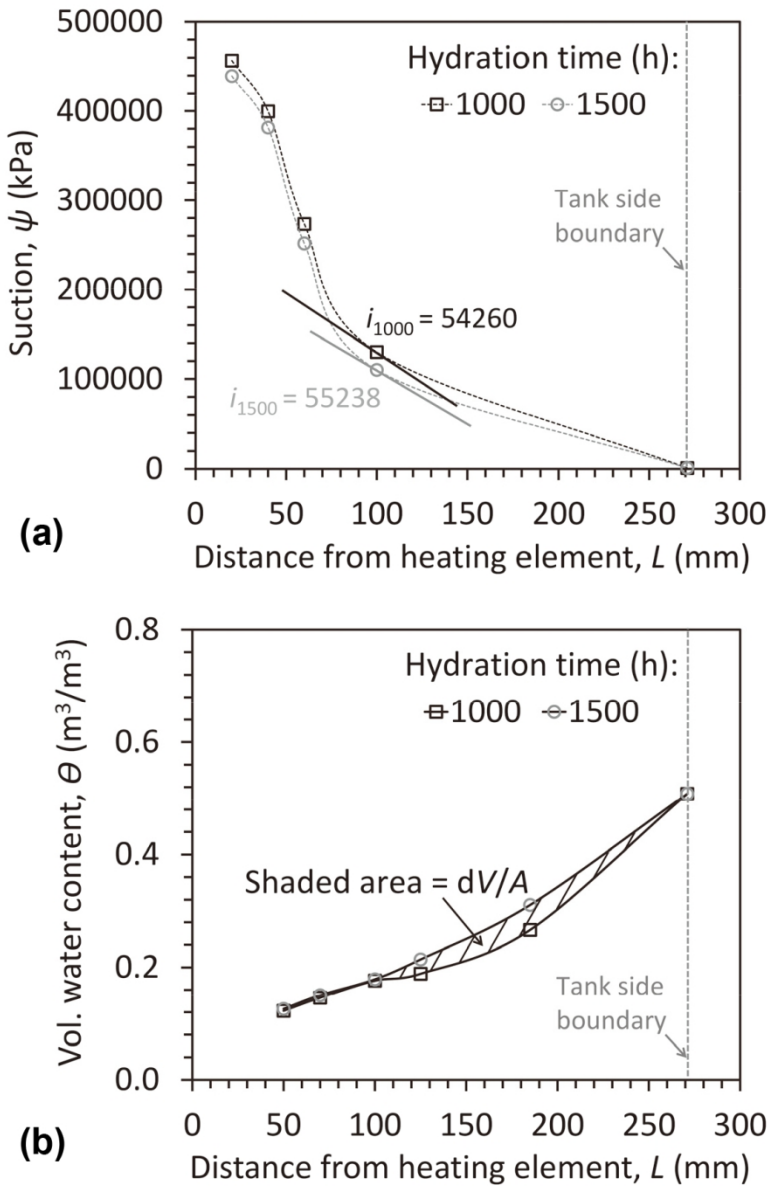

Figure 9. Determination of hydraulic gradient and water flux between two hydration times (e.g., 1000 and 1500 h): (a) Hydraulic gradient; (b) Water flux

88x137mm (330 x 330 DPI)

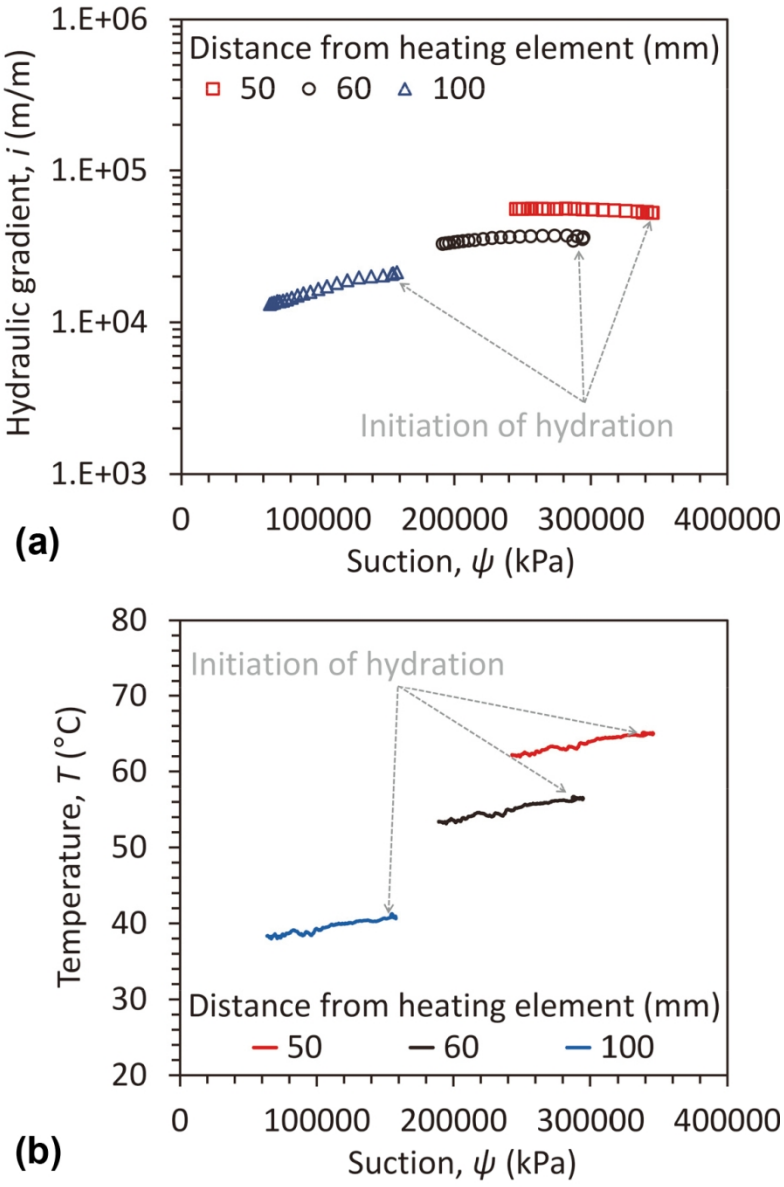

Figure 10. Hydraulic gradient and corresponding temperature versus suction at different sections: (a) Hydraulic gradient; (b) Temperature

88x135mm (330 x 330 DPI)

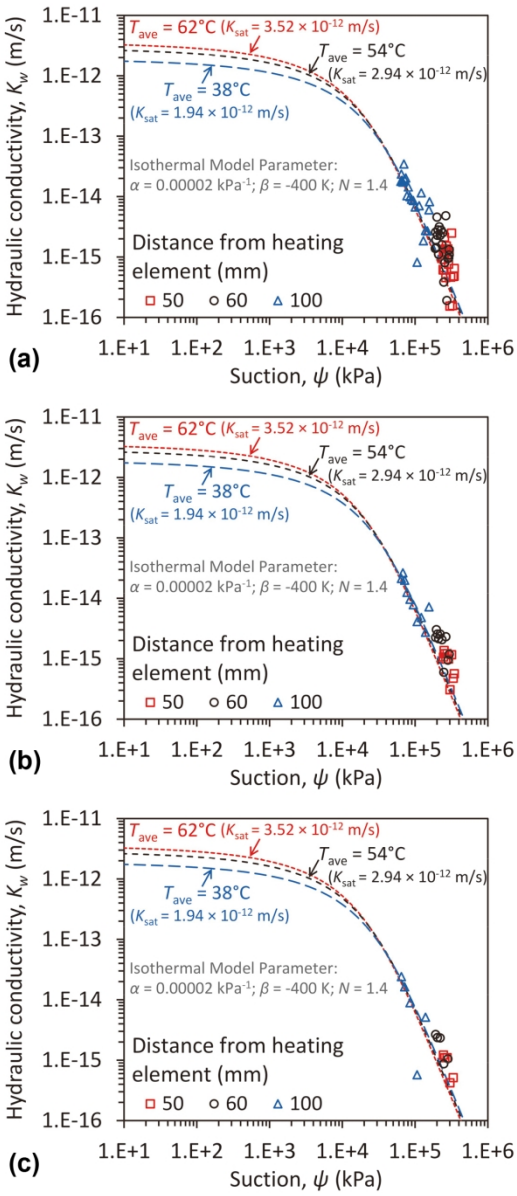

Figure 11. Hydraulic conductivity versus suction data and fitted HCFs for different radial sections having different average temperatures: (a) 200 h interval; (b) 400 h interval; (c) 800 h interval

88x204mm (315 x 315 DPI)

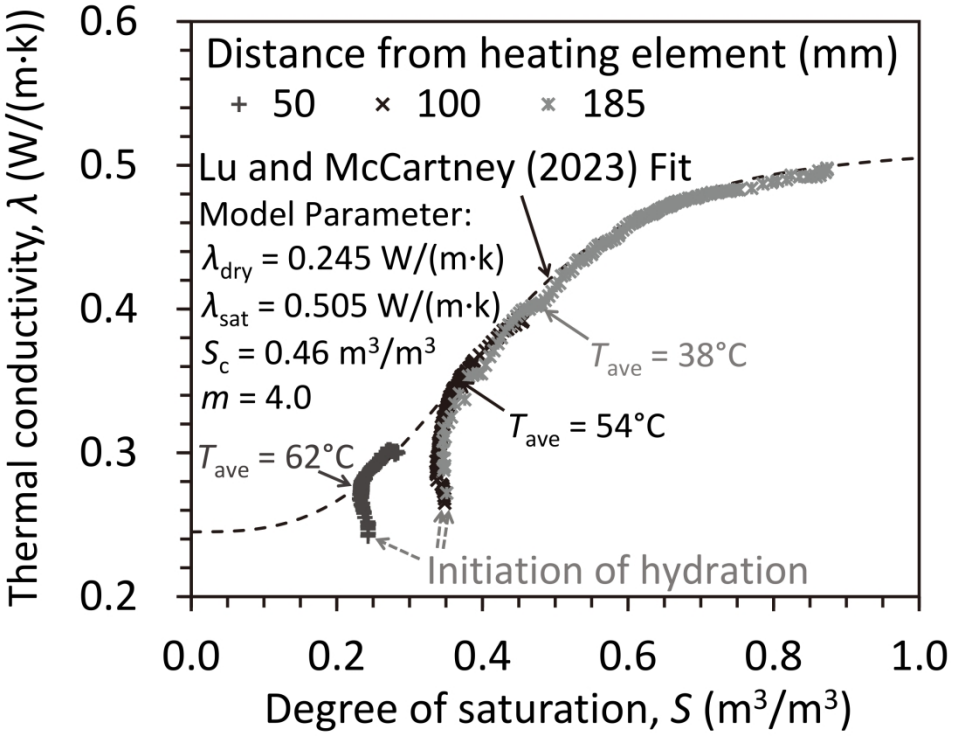

Figure 12. Comparison of measured thermal conductivity at different radial locations and fitted TCF of Lu and McCartney (2023)

88x67mm (773 x 773 DPI)